AIAA 2003-4067

Surface Oil Flow Measurements on Several Airfoils at Low Reynolds Numbers

Bryan D. McGranahan and Michael S. Selig
Department of Aeronautical and Astronautical Engineering
University of Illinois at Urbana–Champaign
Urbana, Illinois 61801

21st AIAA Applied Aerodynamics Conference
June 23–26, 2003/Orlando, FL

Surface Oil Flow Measurements on Several Airfoils at Low Reynolds Numbers

Bryan D. McGranahan[*] and Michael S. Selig[†]

Department of Aeronautical and Astronautical Engineering
University of Illinois at Urbana–Champaign
Urbana, Illinois 61801

Measurements made of upper-surface flow features on the following airfoils is presented: E387, FX 63-137, NASA NLF(1)-0414F, S822, S8036, SD7003, and SD7037 at Reynolds numbers of 200,000, 350,000, and 500,000. Oil-flow visualization of the upper-surface flow features is discussed in detail and comparisons are made between present work and data acquired at the NASA Langley Low-Turbulence Pressure Tunnel (LTPT). Drag polars for the airfoils tested at Reynolds numbers of 200,000, 350,000, and 500,000 are presented allowing a direct comparison between surface flow features and airfoil performance. Also presented is a comparison of upper-surface flow features computed by XFOIL with those measured in the UIUC wind tunnel for Reynolds numbers of 200,000, 350,000, and 500,000.

Introduction

The existence of laminar separation bubbles on low Reynolds number airfoils is one of the most significant barriers to obtaining high performance in the low Reynolds number regime. The associated increase in drag and loss in lift makes many airfoils that perform well at higher Reynolds numbers unsuitable for low Reynolds number use. In order to design new airfoils optimized for low Reynolds number applications, it is necessary to properly analyze the behavior of laminar separation bubbles over a range of conditions.

Currently, there are limited experimental data documenting the location and length of the laminar separation bubbles on airfoils at low Reynolds numbers making it difficult to fully validate computational methods. The purpose of this paper is therefore to provide a source of experimental surface oil-flow measurements of the length and location of laminar separation bubbles on several airfoils over a range of conditions. It is envisioned that this data set will be useful in refining and validating computational models and methods used for low Reynolds number airfoil design and analysis.

Wind Tunnel Facility and Models

All experiments were conducted in the University of Illinois at Urbana–Champaign (UIUC) subsonic wind tunnel, which has a nominal test section that is 2.81-ft high and 4-ft wide. The test set-up depicted in Fig. 1 was used for this study.[1,2] As shown in Fig. 1, two 6-ft

long Plexiglass splitter plates are inserted 2.8 ft apart into the test section to isolate the airfoil models from both the support hardware and the tunnel side wall boundary layers. The 1-ft chord airfoil models were inserted horizontally between the splitter plates with nominal gaps of 0.040–0.080 in. between the end of the airfoil model and the splitter plates. The upper end of the test Reynolds number range was 500,000 and the turbulence intensity of the tunnel with an empty test section was less than 0.1%.[1] The lift was measured using a strain gauge load cell, and the drag was determined using the momentum deficit method.[1] To account for spanwise drag variations at low Reynolds numbers,[3] the drag was obtained from an average of eight equidistant wake surveys over the center of the model so that a 10.5-in. wide span was covered. The overall uncertainty in both the lift and drag measurements was estimated at 1.5%.[1,2] All lift and drag measurements were corrected for wind tunnel interference and validated with data from the NASA Langley Low Turbulence Pressure Tunnel.[1,3–5]

The wind tunnel tests include a broad variety of airfoils, from those designed for use at low Reynolds numbers to airfoils that do not perform well at low Reynolds numbers. Table 1 summarizes the airfoils tested and their significance. Later, suffixes are added to the airfoil names (e.g. '(E)') and used in the captions to indicate the wind-tunnel model versions of those particular airfoils. For instance, the E387 (E) case is the 5th model of the E387 airfoil in the UIUC collection.

The airfoil models were made of foam cores, structurally reinforced, fiberglassed, then sanded and painted. A coordinate-measuring machine was used to digitize the models.[2] The differences between the nominal and measured coordinates were calculated, al-

Fig. 1 Photograph of wind-tunnel test section with model, splitter plates, and vertically-traversed wake probe array installed.
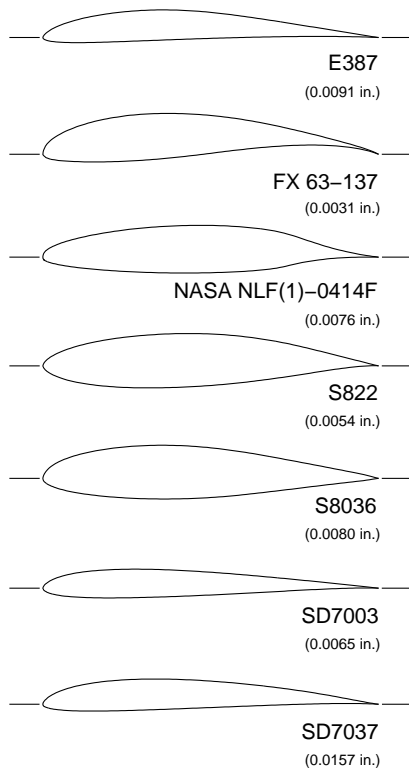

Fig. 2 Airfoils tested and their corresponding average error in inches for the 12-in. chord models presented in this study.

lowing the computation of an average accuracy for each model (mean of the differences). For the airfoils used in the current study, the differences between the nominal and measured coordinates are indicated in Fig. 2 underneath the airfoil names.

Surface Oil Flow Technique

The surface oil flow visualization technique made use of a fluorescent pigment (Kent-Moore 28431-1) suspended in a light, household-grade mineral oil that

Table 1 Airfoils Tested

Airfoil	Significance
E387	Benchmark Eppler airfoil tested in NASA Langley LTPT
FX 63-137	Popular F. X. Wortmann airfoil for high-lift low Reynolds number applications, originally for the Liver Puffin human-powered aircraft (1963)
NLF(1)-0414F	NASA natural laminar flow airfoil that displays degraded performance at low Reynolds numbers; conducive to large bubble formation
S822	Low Reynolds number wind-turbine airfoil, patented by DOE NREL
S8036	Low Reynolds number airfoil designed for soft stall characteristics
SD7003	Designed for low bubble drag at low Reynolds numbers
SD7037	Popular airfoil used for R/C model sailplanes operating at low Reynolds numbers

was sprayed onto the surface of the model using a Paasche Model VL double-action airbrush. The model was then subjected to 20–45 min of continuous wind-tunnel run time at a fixed Reynolds number and angle of attack. During this period, the oil moved in the direction of the local flow velocity at a rate dependent on the balance of forces dictated by the boundary-layer skin friction coefficient C_f and surface tension of the oil. As a result, regions of the flow could be identified and compared with the NASA Langley Low-Turbulence Pressure Tunnel (LTPT) data.[4,5]

Figure 3 shows a photograph of the surface oil flow pattern made visible under fluorescent light. Figure 4 conceptually illustrates the connection between the salient surface oil flow features and the skin friction distribution. Note that the skin friction distribution, though conceptual, is consistent with the results of many computational studies.[6–11] The authors believe that the unique shape of the C_f distribution, in particular the strong negative C_f spike, has yet to be experimentally verified (as no experimental data could be found); however, the oil flow patterns observed seem to confirm the validity of the negative C_f spike concept.
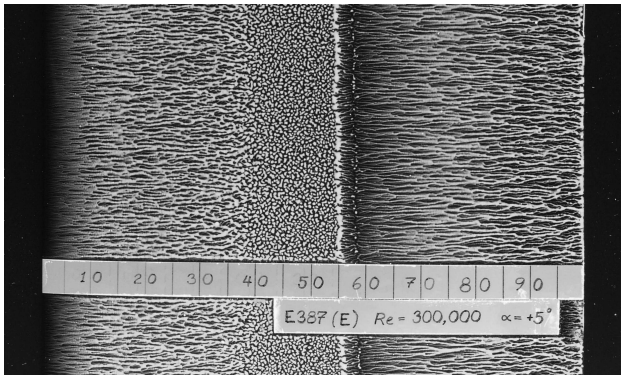
Fig. 3 Representative upper-surface oil flow visualization on the E387 (E), $Re = 300{,}000$, $\alpha = 5$ deg.

Several important flow features can be identified and related to the underlying skin friction and surface tension forces. In Fig. 3, laminar flow is seen to exist from the leading edge to approximately $0.40c$. The oil streaks are characteristically smooth in this region until laminar separation occurs, which is identified in Fig. 4 as the point where $C_f = 0$. (Note again that the flow shown in Fig. 4 is conceptual, and it is not intended to match Fig. 3 in detail.) Downstream of the point of laminar separation, the original airbrushed "orange-peel" texture that existed prior to running the tunnel still exists, indicating that the flow is stagnant in this region. This stagnant flow is consistent with the known behavior of flow in the interior leading-edge region of a laminar separation bubble. As sketched, the C_f magnitude in this region is quite small due to the low flow speed and negative in sign due to reverse flow at the surface.

In the presence of a laminar separation bubble, transition takes place in the free shear layer above the surface of the airfoil. Downstream of this point, reattachment occurs in a process that is known to be unsteady as vortices are periodically generated and impinge on the airfoil surface.[11,12] These unsteady vortices colliding with the surface lead to a relatively high shear stress that tends to scour away the oil at the mean reattachment point, pushing oil upstream or downstream of the reattachment point. As seen in Fig. 4, the reattachment line is less distinct because the bulk of the oil has been pushed away revealing the underlying black airfoil surface. In Fig. 3, the tunnel run time was long enough that the reattachment line at $0.58c$ is even harder to see than in Fig. 4. In the original high-resolution color photographs that were archived, this feature is clear and easily quantifiable.

Downstream of reattachment the boundary layer is turbulent. The high skin friction in this area relative to the laminar boundary layer upstream tends to clear away more oil, again making the black surface downstream more visible than in the upstream region.

The remaining visible feature of the flow is a line where the oil tends to pool, termed here the "oil accu-
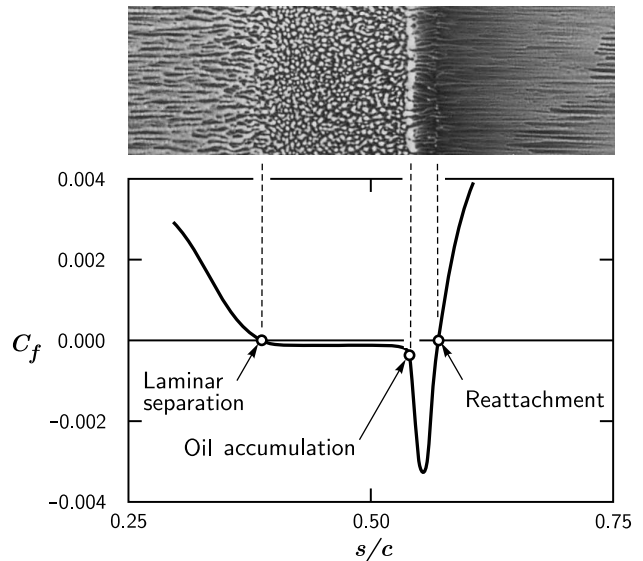

Fig. 4 Conceptual illustration of the relationship between the surface oil flow features and skin friction distribution in the region of a laminar separation bubble plotted against the airfoil arc length coordinate s/c.

mulation line." This intrinsic feature of the oil flow has no direct connection to laminar flow, reverse flow in the bubble, or the ensuing turbulent flow downstream. However, it does indicate a relatively important feature of the flow with regard to the nature of the skin friction in the vicinity of reattachment. The negative C_f spike shown in predictions and sketched conceptually in Fig. 4 is most likely responsible for generating the oil accumulation line. Assuming that this is the case, the fluctuating high skin friction that is generated over the unsteady reattachment zone will tend to push the oil upstream ahead of the mean reattachment point. At some location on the airfoil, however, the oil moving upstream will experience a balance of forces between the rapidly weakening skin friction force and that of the surface tension and oil adhesion that is retarding its motion. At the location where these two forces balance, the oil accumulates into a line that becomes the most distinguishable feature of the oil flow. Consequently, it is speculated that this flow feature is sometimes mislabeled as "reattachment" as will be discussed below.

Figures 5 and 6 show the previously described flow features compared with data obtained at the NASA Langley LTPT. In the low drag range between -2 deg and 7 deg angle of attack, the agreement in the laminar separation line between the NASA LTPT and UIUC data sets is mostly within $0.01c$ to $0.02c$, which is very near the uncertainty of the method. As previously discussed, the next feature to appear is the oil accumulation line. The UIUC oil accumulation line agrees fairly well with the "reattachment" line identified in the NASA experiment. It is believed, however,

that based on the previous reasoning this label given in the original reference[5] is a misnomer. Had the UIUC tests been performed for a longer duration, the reattachment zone would be scoured clean with no distinguishing feature, leaving only the oil accumulation line to be labeled as the "reattachment line," knowing that one must exist. Hence, it is speculated here and in prior UIUC work[2] that such a scenario took place in the NASA study, i.e. the oil-accumulation line was misinterpreted as the reattachment line.

Guided by this working assumption, the two results again are in good agreement. It must be stated, however, that the oil accumulation line might change slightly from one facility to the next since it is dictated by a force balance that depends on the skin friction forces of the boundary layer relative to the adhesion forces of the particular oil used. The predictions, however, show that the negative C_f region has a sharp upstream edge, which is most likely where the oil accumulates regardless of the surface tension characteristics. Differences in the oil accumulation line due to differences in the type of oil used are therefore believed to be small. The good comparisons between UIUC and Langley data tend to support this assumption.

Moving further downstream, the UIUC reattachment data is plotted, but unfortunately no direct comparison can be made because of the ambiguity with respect to the reattachment data reported in the NASA study. However, close inspection of the data suggests that at a Reynolds of 300,000 and between 5 deg and 7 deg angle of attack, the LTPT line merges with the UIUC reattachment line. Perhaps in this case, the measurements at Langley were indeed the reattachment points.

The conclusion to be drawn from this comparison of the oil flow visualization results is that the two facilities produce airfoil flows that are in close agreement. Moreover, if the arguments regarding the oil accumulation line are correct, then the agreement can be considered excellent and within the uncertainty of the measurements.

It is worth mentioning that during these tests surface oil flow data were not taken at a Reynolds number of 100,000 because the run times would be in excess of 2 hrs per data point. Over this period of time, the droplets of oil spray that initially give rise to the 'orange peel' texture tend to smooth out, which reduces the contrast between the different regions of the flow, thereby making it difficult to ascertain the distinguishing features of the flow.

Computational Methods

The upper-surface flow features for each airfoil were computed at Reynolds numbers of 200,000, 350,000, and 500,000 and at angles of attack from −2 to 18 deg using XFOIL[13] (version 6.94). XFOIL uses a linear-
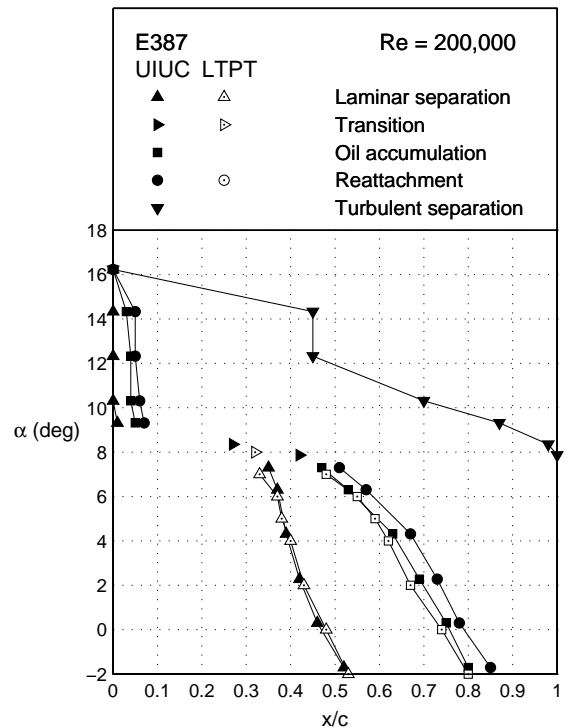

Fig. 5   Comparison of major E387 (E) upper-surface flow features between UIUC and LTPT for $Re = 200,000$.
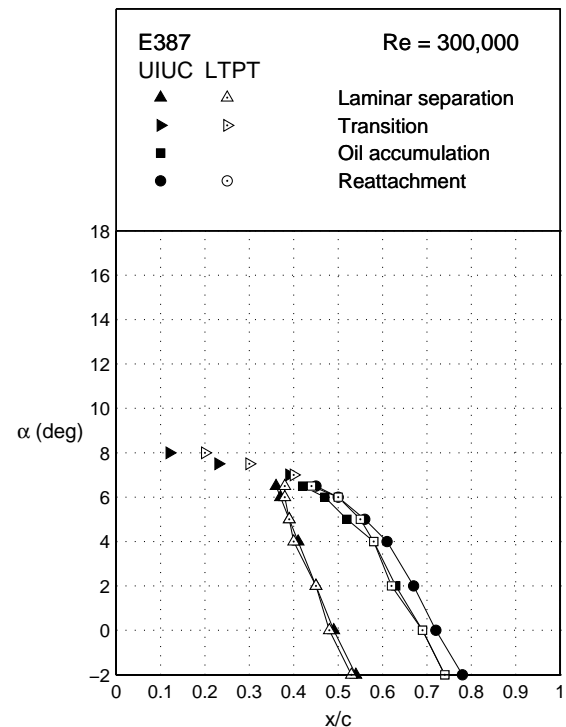

Fig. 6   Comparison of major E387 (E) upper-surface flow features between UIUC and LTPT for $Re = 300,000$.

vorticity panel method for inviscid analysis coupled with an integral boundary-layer method for viscous analysis. The suitability of XFOIL for use in the presence of significant transitional separation bubbles has been demonstrated.[13]

The chordwise location of transition from laminar to turbulent flow x_{tr} is computed by XFOIL using an envelope e^n-type method. For the current work n_{crit} was set to the default value of 9, which is typical for a smooth wing surface in a low-turbulence environment. Each airfoil was represented in XFOIL using 230 panels distributed using XFOIL's default paneling routine.

The skin friction coefficient at each airfoil x-y coordinate was computed for each combination of Reynolds number and angle of attack. At the point of laminar separation, the value of C_f is zero and immediately downstream it becomes negative. The value of C_f remains negative until the flow reattaches behind the laminar separation bubble, at which point C_f again becomes positive. Determining the extent of the separation bubble is accomplished by reading in the XFOIL output file and testing each value of C_f until a change of sign is encountered. In this way, both the extent of the laminar separation bubble and the chordwise location of turbulent separation could be measured. In order to resolve the location of the laminar separation bubble beyond that of the airfoil panel spacing, a linear interpolation for $C_f = 0$ was used to calculate the chordwise location based on the values of skin friction on either side of the sign change. In the vicinity of the ends of the separation bubble, the change in C_f is continuous, and the linear approximation is judged to be sufficient to resolve the chordwise location of laminar separation within the range of the experimental accuracy of the wind-tunnel data.

Results and Discussion

Figures 7–13 show the location of the upper surface laminar separation bubble at Reynolds numbers of 200,000, 350,000, and 500,000 for each airfoil. To make the legends more compact, the Reynolds numbers are abbreviated, e.g., 500,000 is reduced to "500k." As can be seen in the figures, over the range of angles of attack tested, there are three characteristic regions that can be distinguished by changes in the behavior of the bubble. For instance, consider the E387 airfoil (Fig. 7). At low angles of attack, the upper surface is dominated by a large laminar separation bubble approximately centered about the mid-chord of the airfoil. As the angle of attack is increased, the bubble moves toward the leading edge of the airfoil, with the length of the bubble gradually decreasing. On certain airfoils this forward progression continues all the way to the leading edge of the airfoil and the bubble gradually decreases in length until it ultimately terminates in a very small leading edge bubble. On airfoils such

as the E387, there is a region near the upper edge of the polar where the bubble disappears completely and transition to a turbulent boundary layer occurs without a bubble (denoted as "Transition" in the legends). This case typically only occurs over a narrow range of angles of attack as the transition location rapidly moves toward the leading edge of the airfoil. As the angle of attack is further increased, a point is reached where the flow once again gives way to the formation of a laminar separation bubble. This "leading edge bubble" is much shorter than the mid-chord bubble, typically only $0.05c$ to $0.08c$. Because the curvature of the leading edge is much greater than that of the mid-chord region, the leading edge bubble moves very little in the chordwise direction as it curves around the leading edge of the airfoil. The leading edge bubble stays virtually unchanged throughout the rest of the angle of attack range until the airfoil is fully stalled.

The most prominent Reynolds number effect is that the length of the mid-chord laminar separation bubble tends to decrease as the Reynolds number is increased. This is consistent with the fact that laminar separation bubbles typically only appear at low Reynolds numbers. At the lowest Reynolds number tested, the mid-chord separation bubbles are quite long, often covering $0.20c$ to $0.30c$ for the airfoils tested. As the Reynolds number increases, the bubble gradually decreases in size, with the line of laminar separation moving toward the trailing edge of the airfoil and the reattachment line moving toward the leading edge of the airfoil. Certain airfoils, such as the FX 63-137
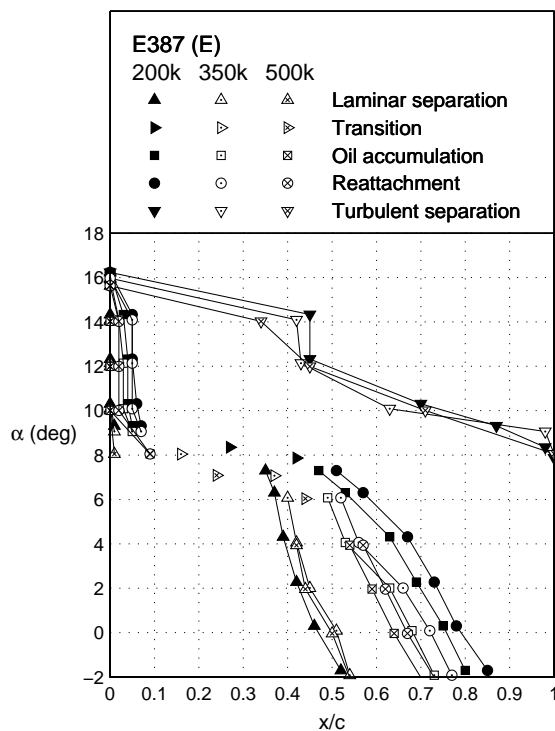

Fig. 7 Locations of upper surface flow features for the E387 (E) airfoil.
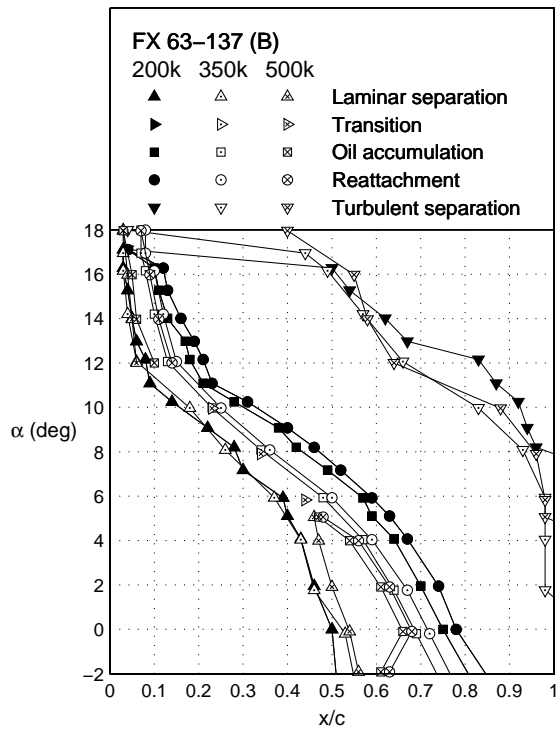
Fig. 8   Locations of upper surface flow features for the FX 63-137 (B) airfoil.
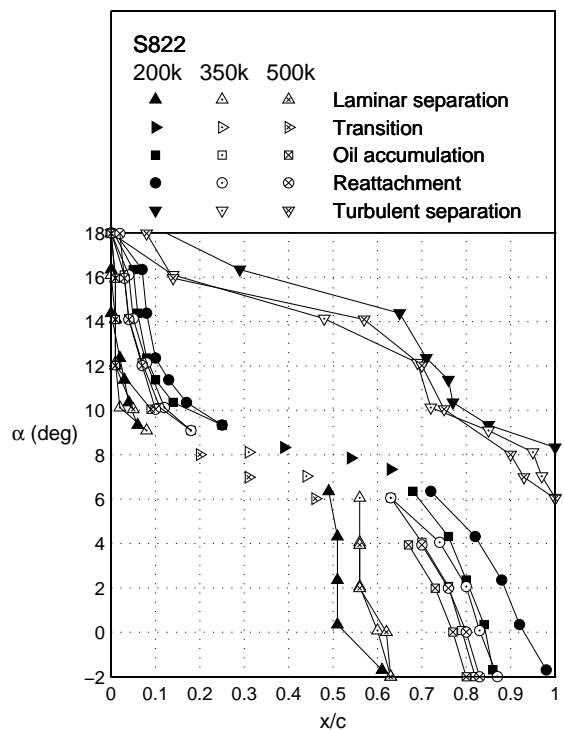

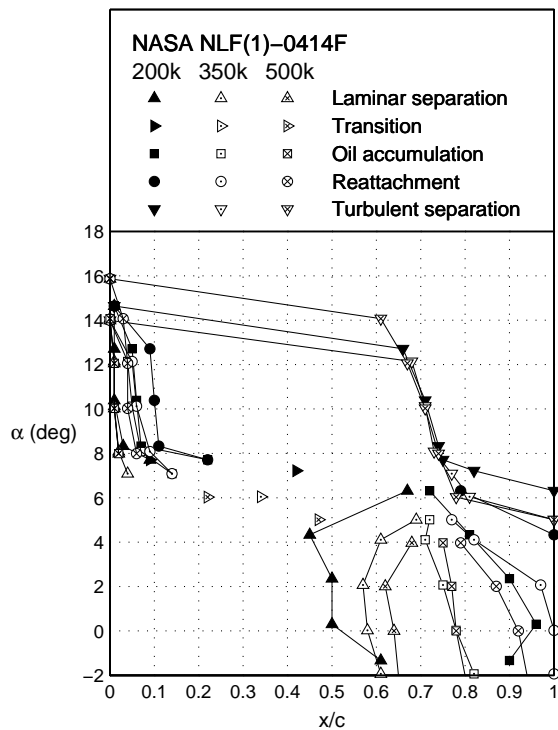Fig. 10   Locations of upper surface flow features for the S822 airfoil.

Fig. 9   Locations of upper surface flow features for the NASA NLF(1)-0414F airfoil.
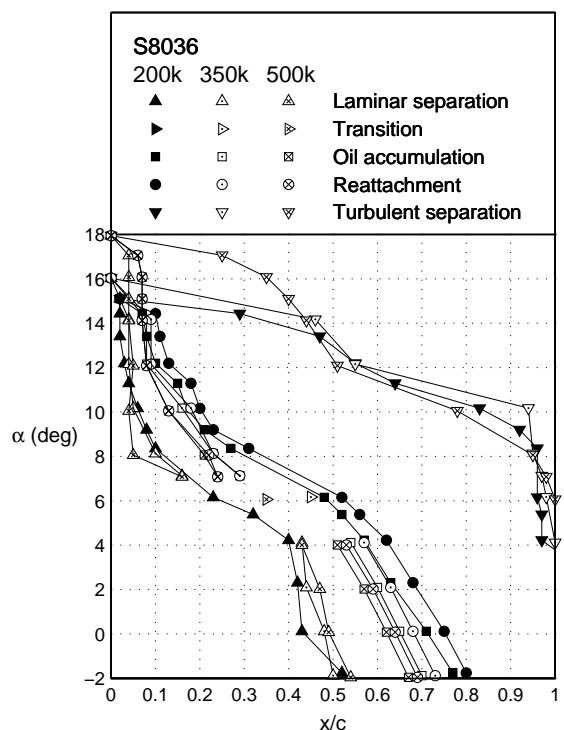

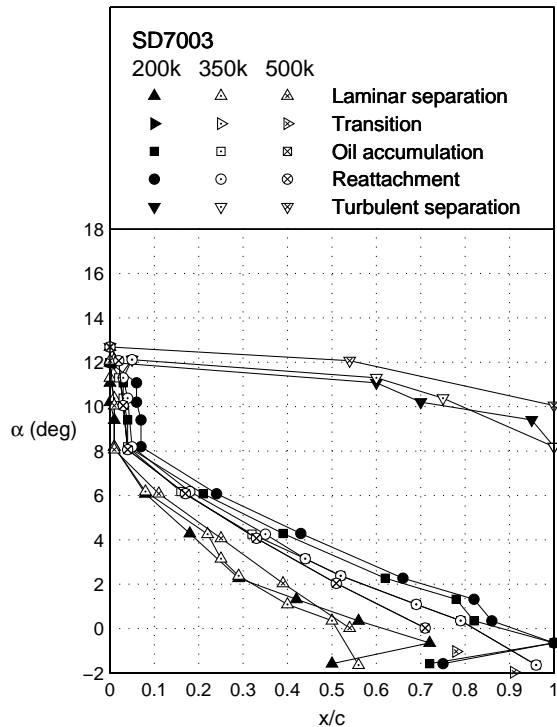Fig. 11   Locations of upper surface flow features for the S8036 airfoil.

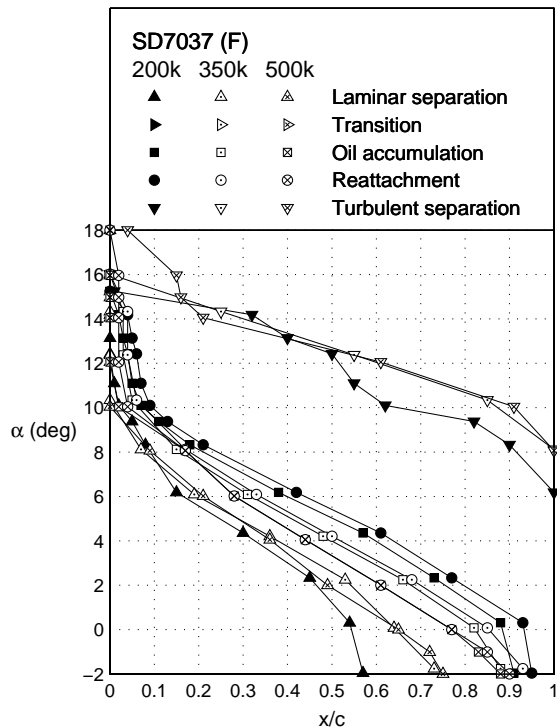**Fig. 12 Locations of upper surface flow features for the SD7003 airfoil.**

Fig. 13 Locations of upper surface flow features for the SD7037 (F) airfoil.

shown in Fig. 8 exhibit transition without a bubble over a range of angles of attack at higher Reynolds numbers, while at lower Reynolds numbers the bubble exists throughout the operating range. Airfoils such as the SD7003 and SD7037 (seen in Figs. 12 and 13 respectively) on the other hand, maintain a laminar

separation bubble over the entire range of Reynolds numbers and angles of attack tested. The length of the bubble diminishes as the Reynolds number increases, but even at the highest Reynolds number tested, the bubble remains until the airfoil stalls.

Assuming that the oil accumulation line is caused by a negative C_f spike as asserted, the region between the oil accumulation line and the reattachment line can give some insight into the strength of the laminar separation bubble. Airfoils with a relatively large distance between the oil accumulation line and the reattachment point, such as the NLF(1)-0414F in Fig. 9, are poor low Reynolds number performers. Airfoils tested that do perform well at low Reynolds numbers, the SD7003 (Fig. 12) and SD7037 (Fig. 13), start out with a relatively small distance between the oil accumulation line and the reattachment point at low Reynolds numbers, with the distance decreasing as the Reynolds number is increased. The two lines become indistinguishable from each other at high Reynolds numbers. Not all airfoils follow this trend. The E387, for example (Fig. 7), has good low Reynolds number performance and a moderate distance between the oil accumulation line and the reattachment point that neither shrinks nor grows with changes in Reynolds number.

Figures 14–20 show drag polars for the E387 (E), FX 63-137 (B), NASA NLF(1)-414F, S822, S8036, SD7003, and SD7037 (F) at Reynolds numbers of 200,000, 350,000, and 500,000. By comparing the upper surface flow features (Figs. 7–13) and the drag polars (Figs. 14–20), some general trends can be identified. First, as one would expect, the upper corner of the low drag range of the polar generally corresponds with the point when transition either with or without a bubble moves to the leading edge. Thus it may be deduced that the lower corner of the polar is driven by transition moving toward the leading edge. Second, between these "limiting angles of attack," the low drag range of the polar is defined by there being extended runs of laminar flow. However, the performance is somewhat handicapped by there being laminar separation bubbles. Third, the type of stall as characterized by the C_l vs. α curve can be related to the behavior of the surface oil flow features as has been discussion in Ref. 14. These observations are supported by prior investigations and current predictions.

XFOIL Predictions

A comparison between the computational results and the wind tunnel tests for separation bubble length and location can be seen in Figs. 21–41. These results obtained using XFOIL mimic the measured behavior of the airfoils, but there are some important differences. The mid-chord bubble location predicted XFOIL is quite consistent with experiment; however, the length of the bubble can differ considerably from
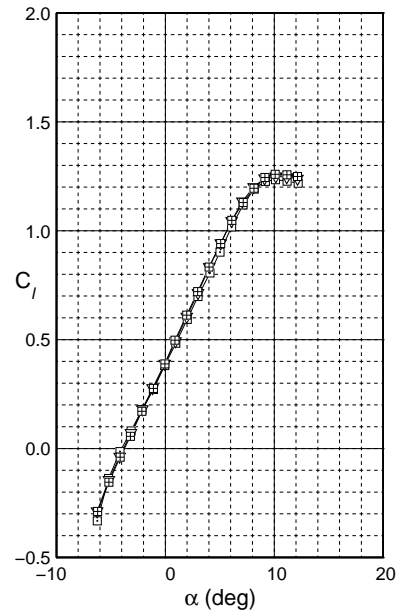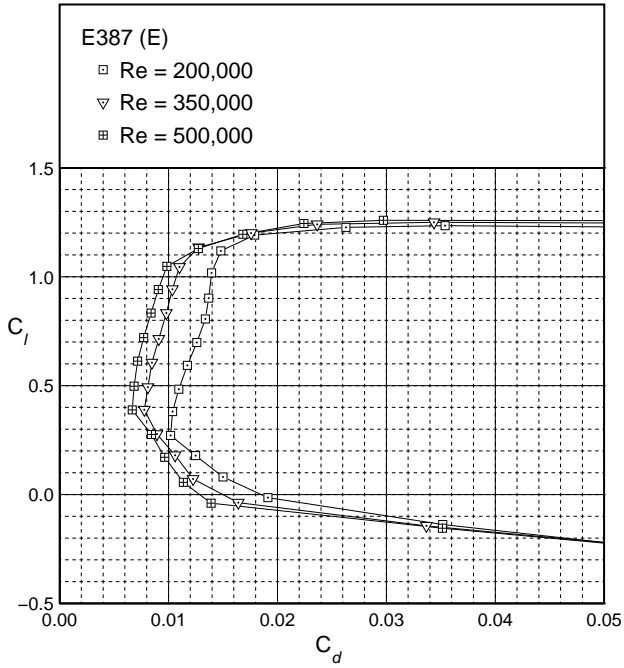
Fig. 14   Experimental lift and drag data for the E387 (E) airfoil.
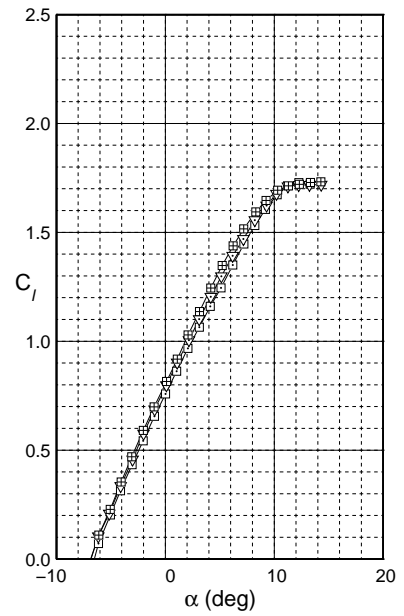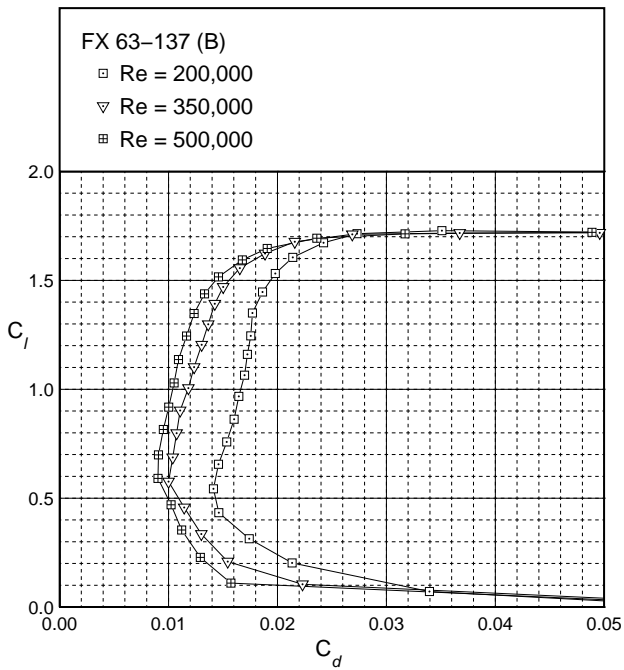

Fig. 15   Experimental lift and drag data for the FX 63-137 (B) airfoil.

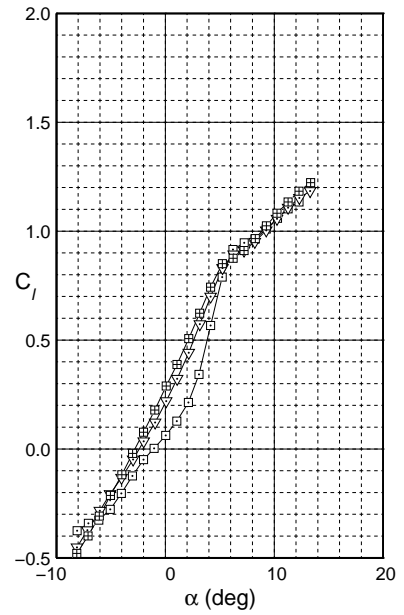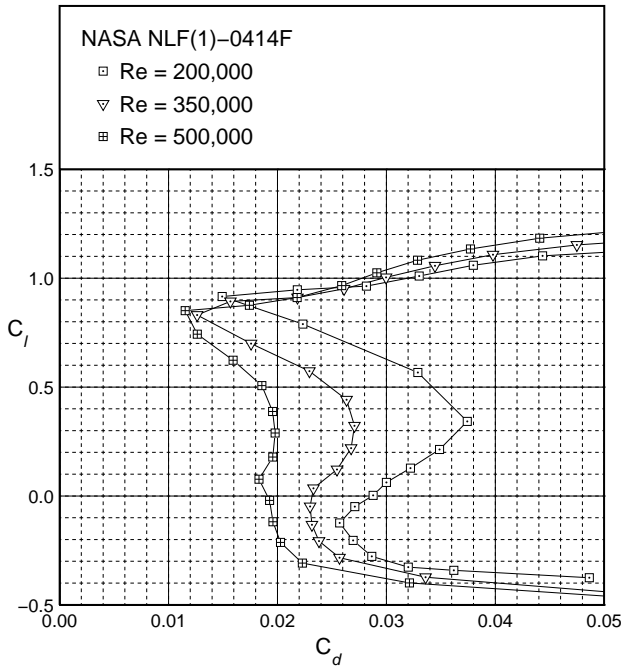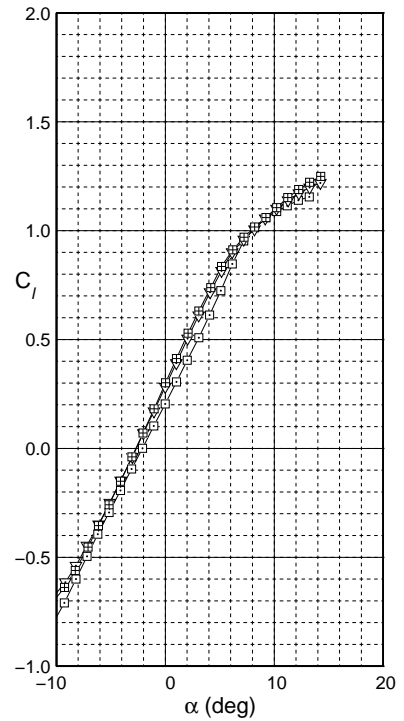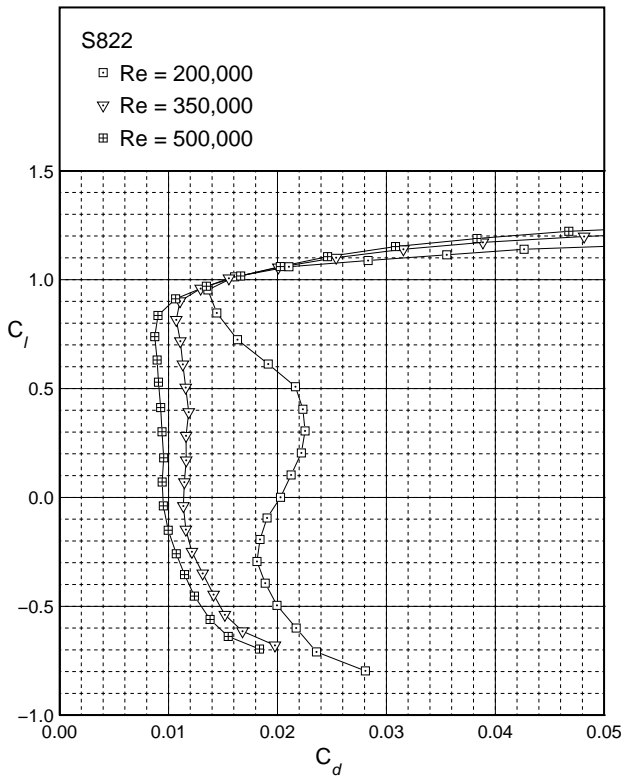**Fig. 16   Experimental lift and drag data for the NASA NLF(1)-0414F airfoil.**
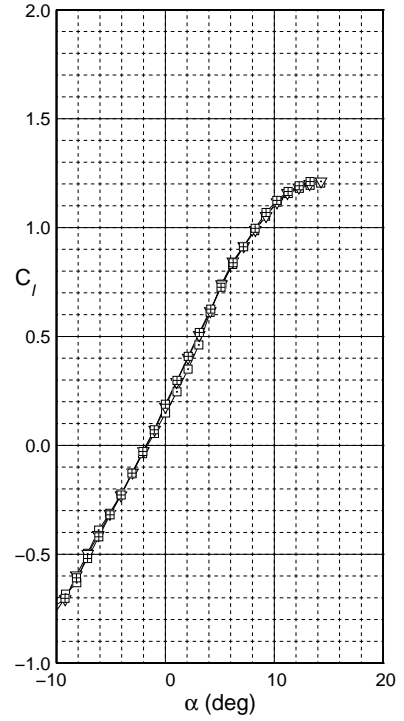

Fig. 17   Experimental lift and drag data for the S822 airfoil.
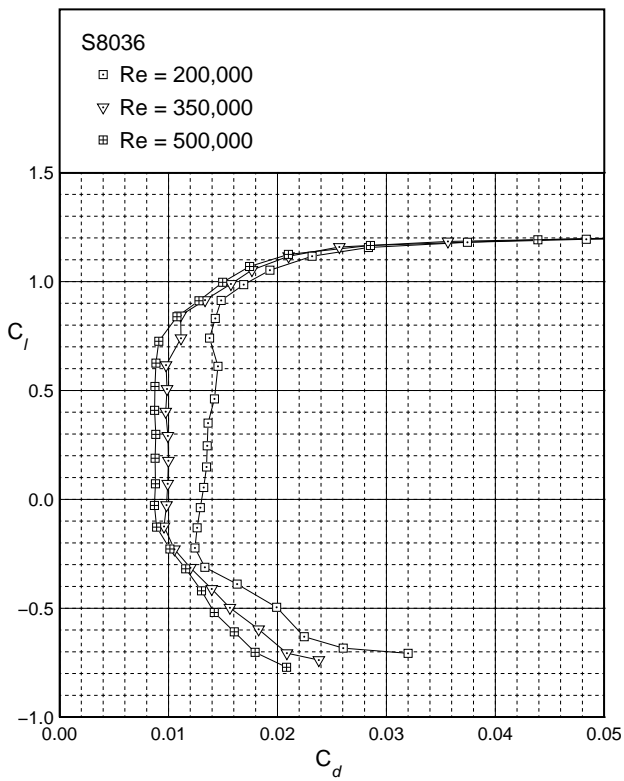
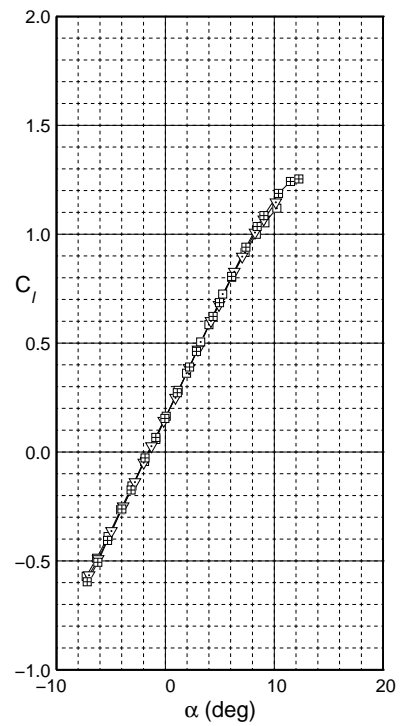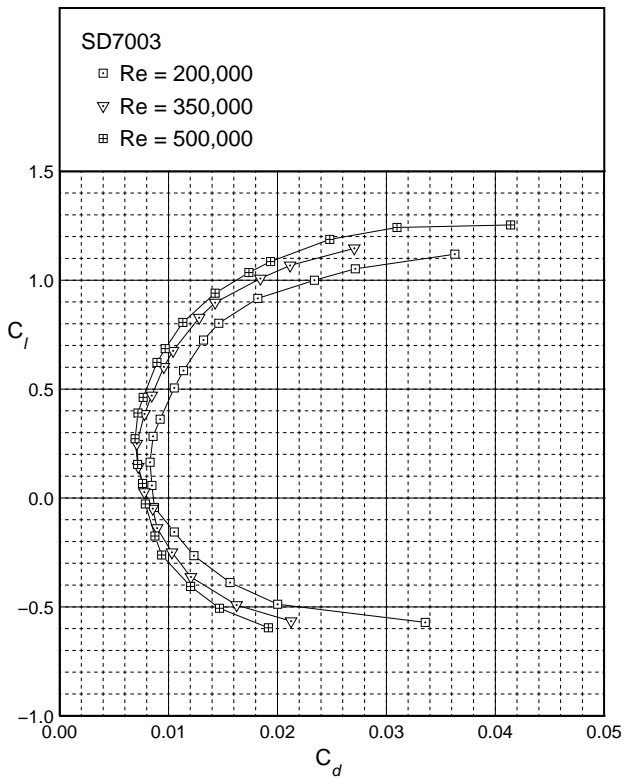**Fig. 18 Experimental lift and drag data for the S8036 airfoil.**

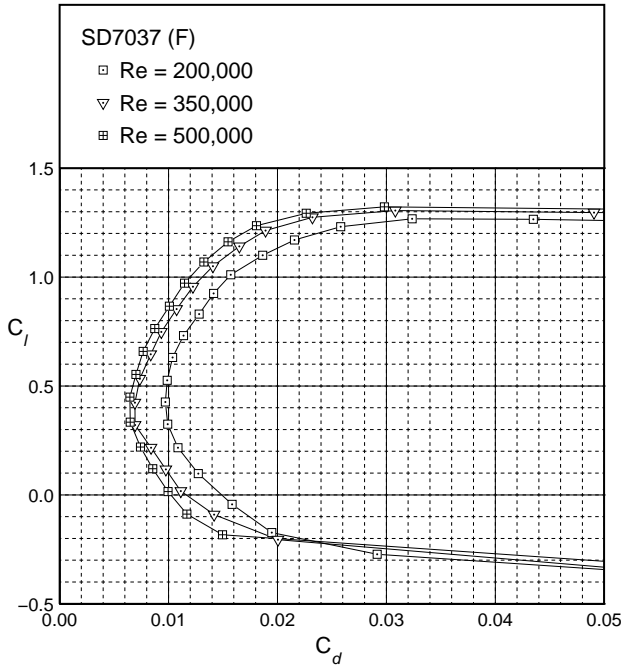**Fig. 19 Experimental lift and drag data for the SD7003 airfoil.**

Fig. 20 Experimental lift and drag data for the SD7037 (F) airfoil.

the length measured in the wind tunnel. XFOIL predictions of the length of the laminar separation bubble are typically $0.05c$ to $0.10c$ shorter than measured. A consequence of the shorter laminar separation bubble predicted by XFOIL is that for airfoils with very weak laminar separation bubbles such as the SD7003 (Figs. 36–38) and the SD7037 (Figs. 39–41), XFOIL incorrectly predicts transition without a bubble even though both airfoils maintain a laminar separation bubble throughout the operational range.

In general XFOIL is more accurate at predicting the reattachment point than it is at predicting the line of laminar separation. For example, the computed reattachment point for the S8036 (Figs. 33–35) lies within $0.01c$ to $0.03c$ of the measured location while the location of the line of laminar separation computed by XFOIL is typically off by $0.05c$ over the same range of angles of attack.

Another area in which XFOIL differs from experiment is in the prediction of turbulent separation. The location of turbulent separation predicted by XFOIL is significantly further aft than that observed in the wind tunnel. For most cases tested, the XFOIL predictions of the chordwise location of turbulent separation differ from experiment slightly as the trailing edge flow first separates, with the discrepancies becoming greater as the angle of attack is increased. This tendency of XFOIL to under-predict the extent of turbulent separation results in a stall angle of attack that is greater than that seen in the wind tunnel data.
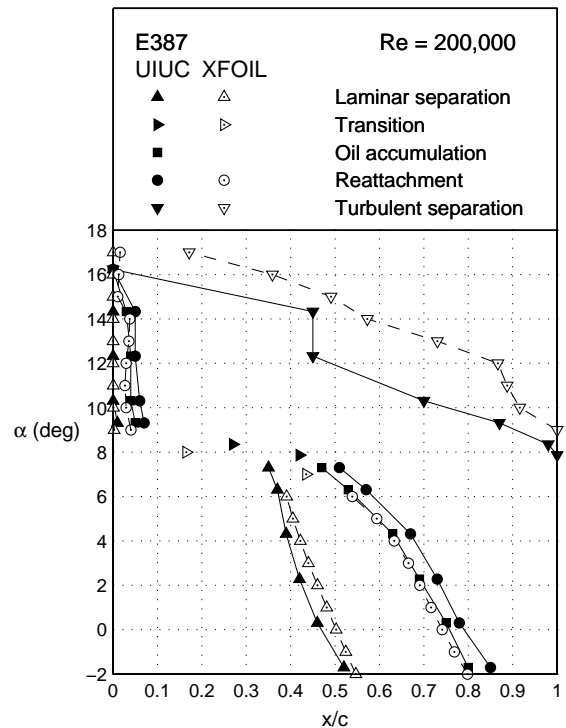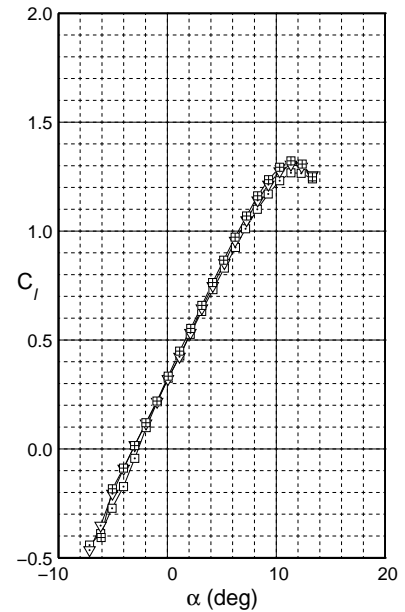
Fig. 21 Comparisons between computational and experimental location of upper surface flow features for the E387 (E), $Re = 200{,}000$.
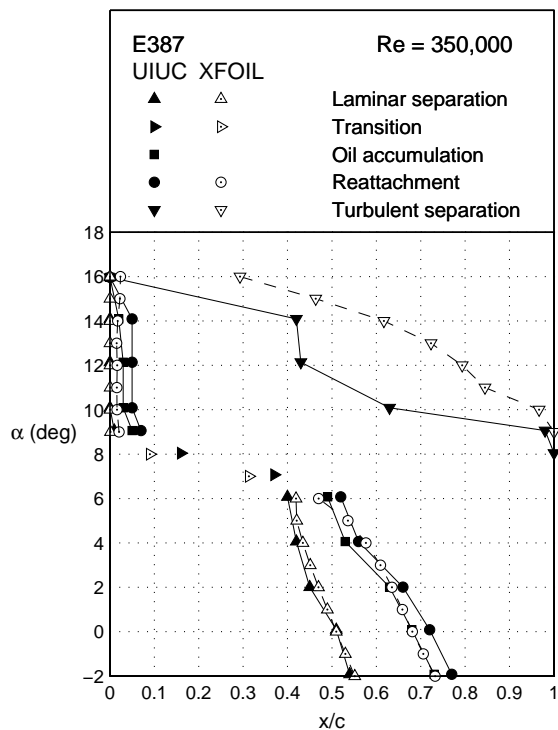
Fig. 22 Comparisons between computational and experimental location of upper surface flow features for the E387 (E), $Re = 350,000$.
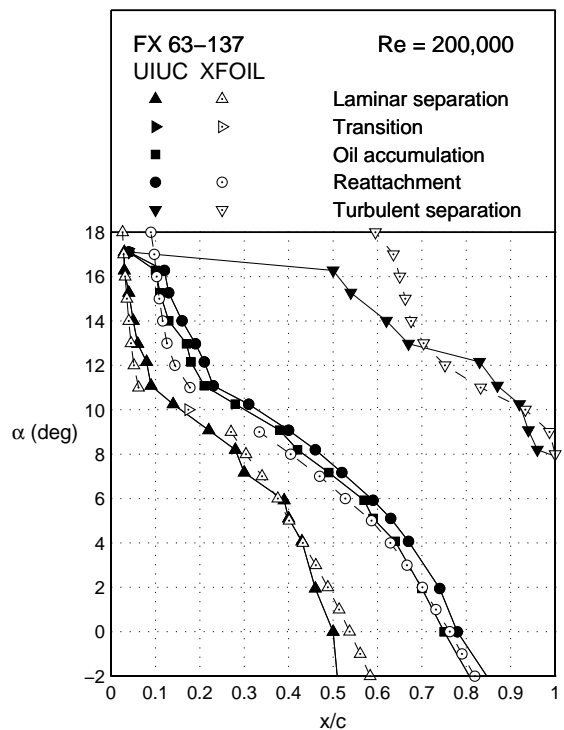

Fig. 24 Comparisons between computational and experimental location of upper surface flow features for the FX 63-137 (B), $Re = 200,000$.
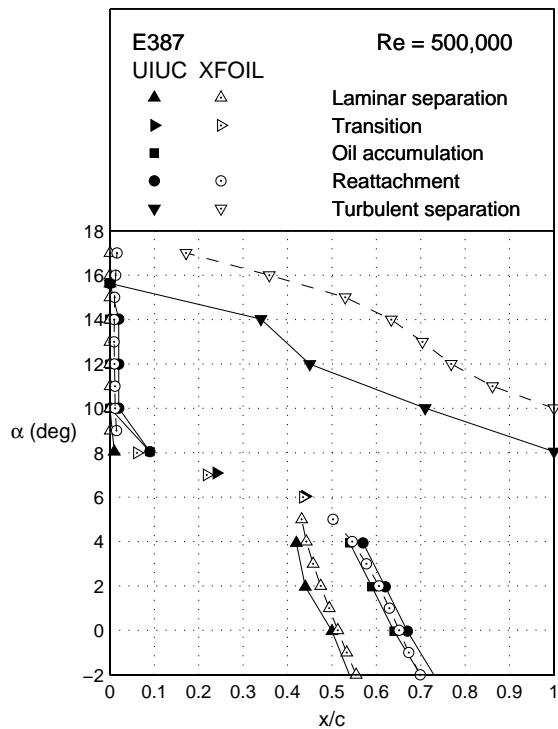

Fig. 23 Comparisons between computational and experimental location of upper surface flow features for the E387 (E), $Re = 500,000$.
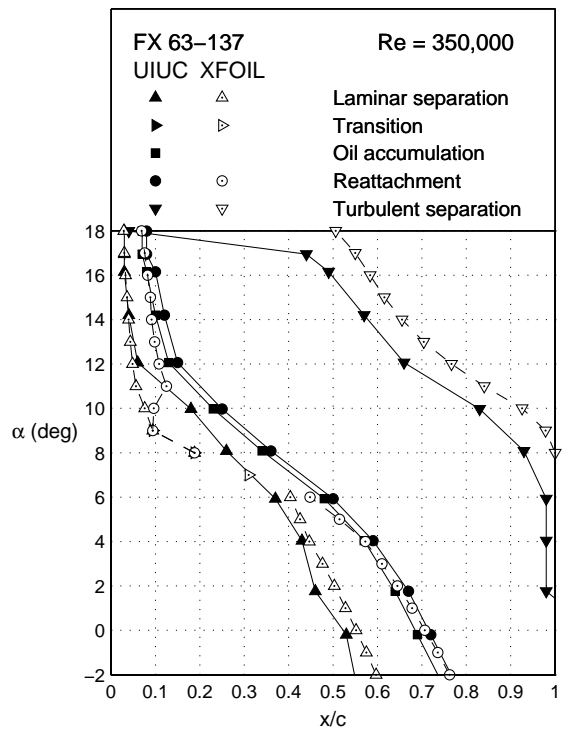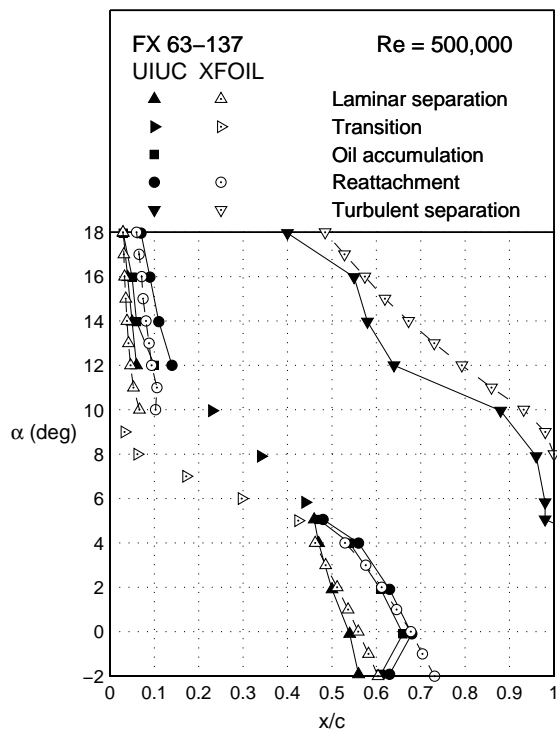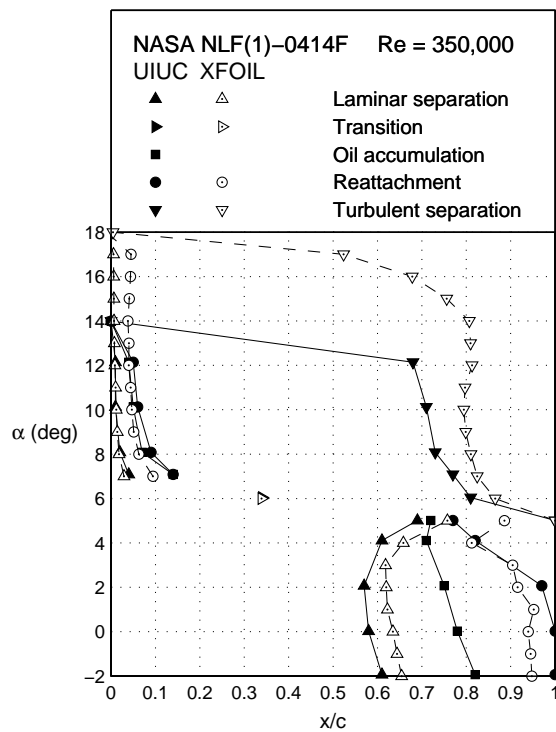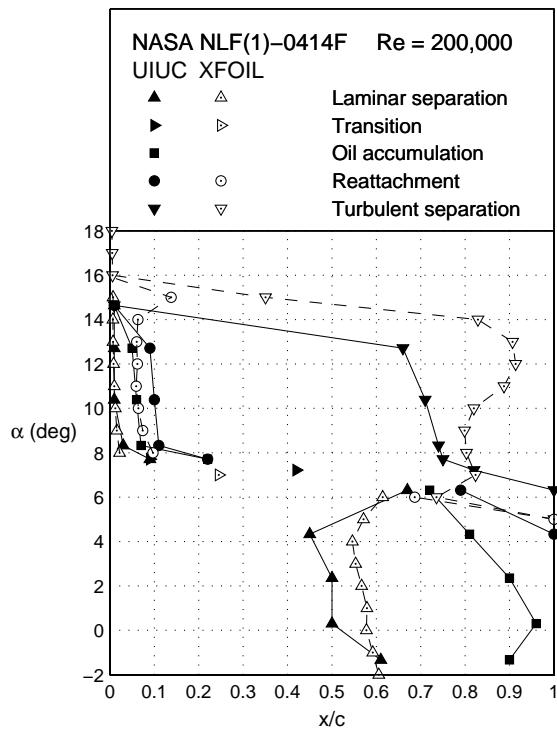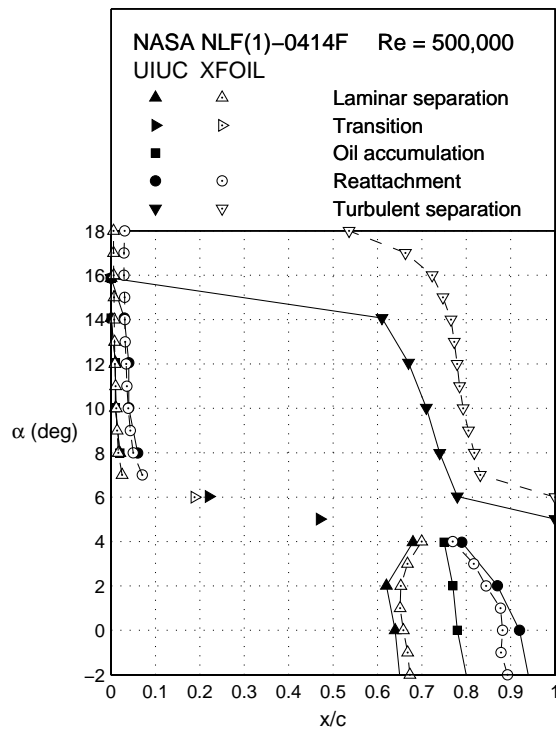

Fig. 25 Comparisons between computational and experimental location of upper surface flow features for the FX 63-137 (B), $Re = 350,000$.

Fig. 26 Comparisons between computational and experimental location of upper surface flow features for the FX 63-137 (B), $Re = 500,000$.

Fig. 28 Comparisons between computational and experimental location of upper surface flow features for the NASA NLF(1)-0414F, $Re = 350,000$.
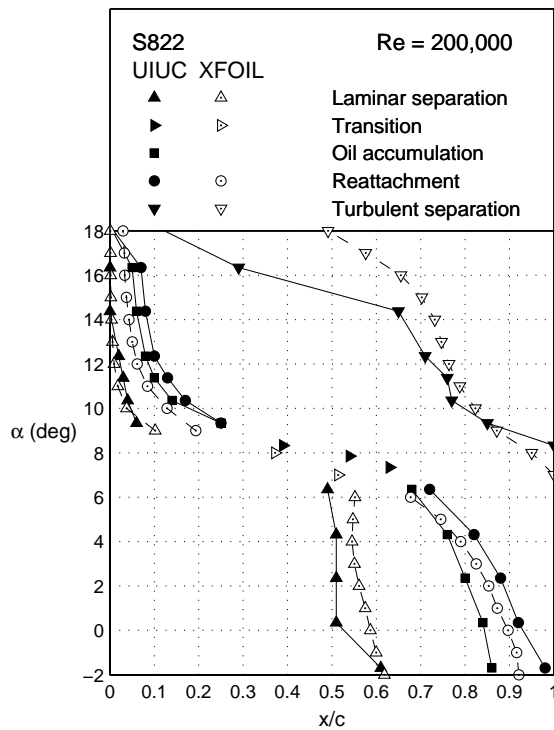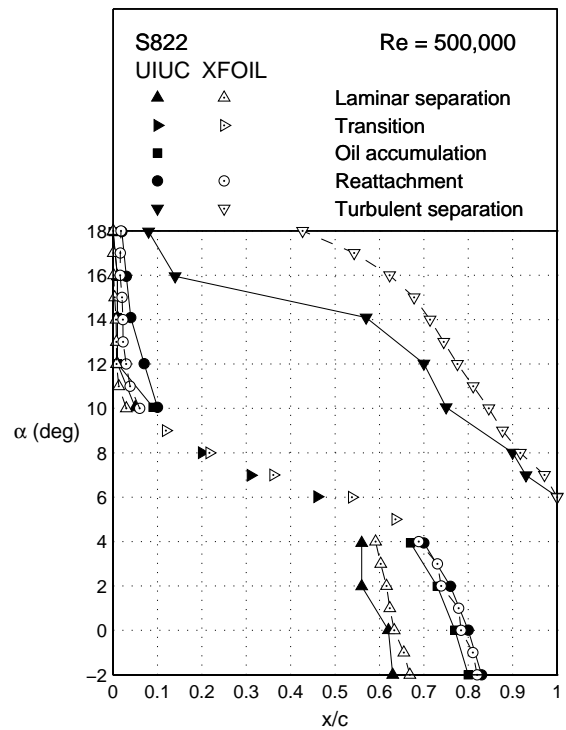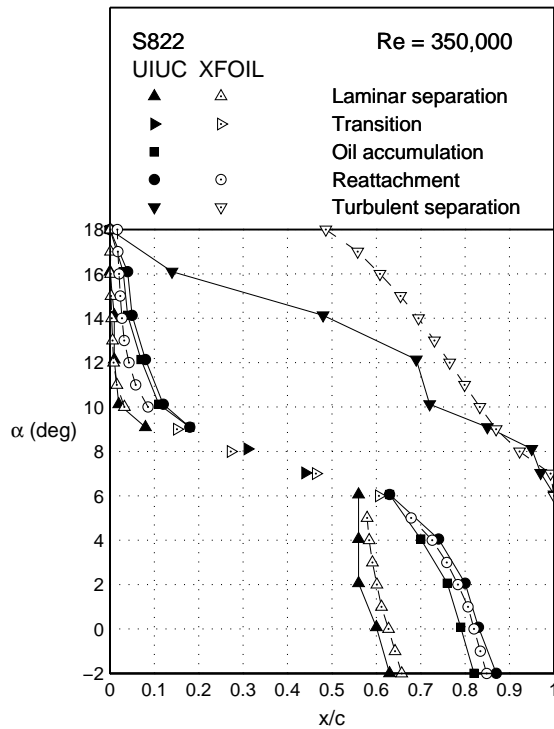

Fig. 27 Comparisons between computational and experimental location of upper surface flow features for the NASA NLF(1)-0414F, $Re = 200,000$.

Fig. 29 Comparisons between computational and experimental location of upper surface flow features for the NASA NLF(1)-0414F, $Re = 500,000$.

Fig. 30 Comparisons between computational and experimental location of upper surface flow features for the S822, $Re = 200,000$.
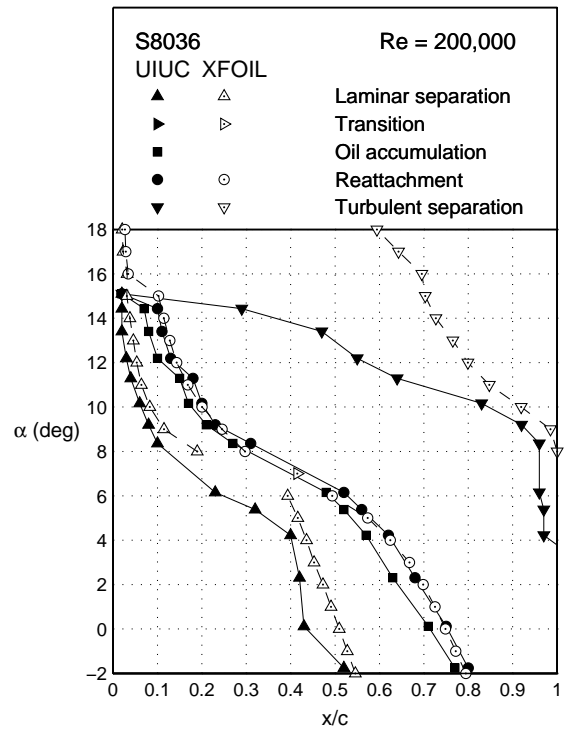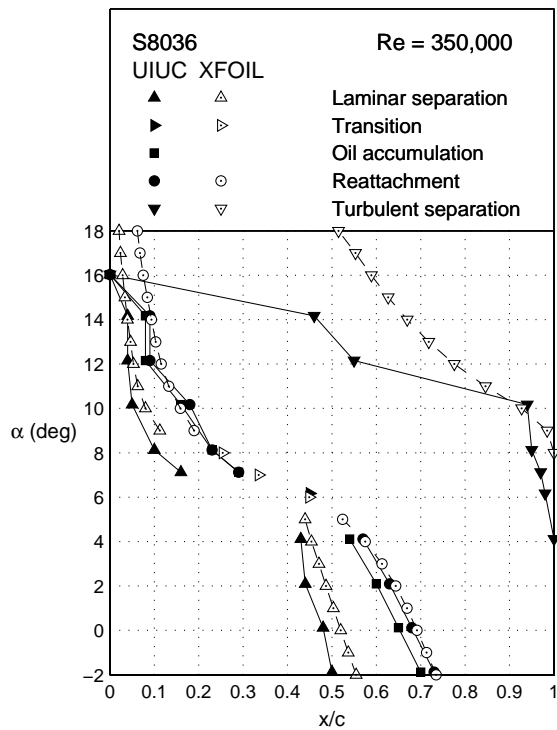

Fig. 32 Comparisons between computational and experimental location of upper surface flow features for the S822, $Re = 500,000$.

Fig. 31 Comparisons between computational and experimental location of upper surface flow features for the S822, $Re = 350,000$.
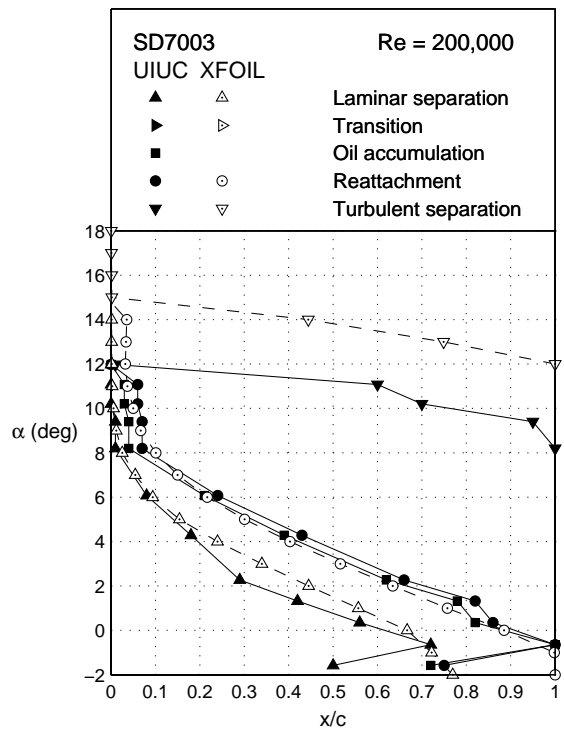

Fig. 33 Comparisons between computational and experimental location of upper surface flow features for the S8036, $Re = 200,000$.

Fig. 34 Comparisons between computational and experimental location of upper surface flow features for the S8036, $Re = 350,000$.

Fig. 36 Comparisons between computational and experimental location of upper surface flow features for the SD7003, $Re = 200,000$.
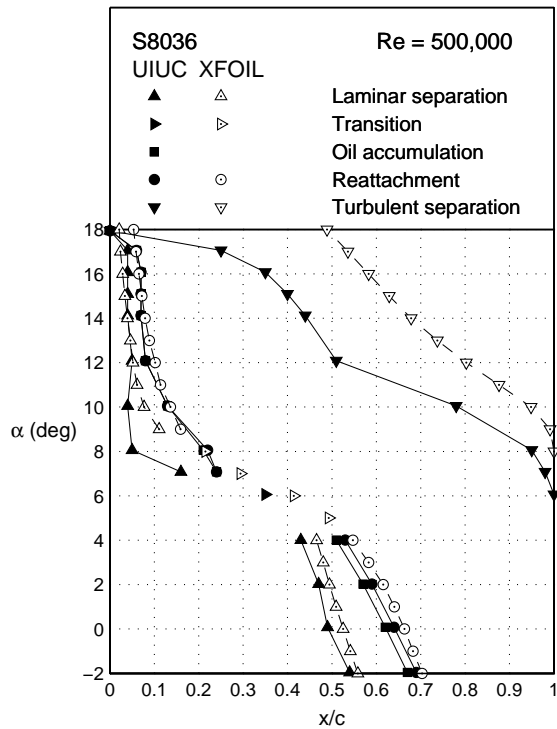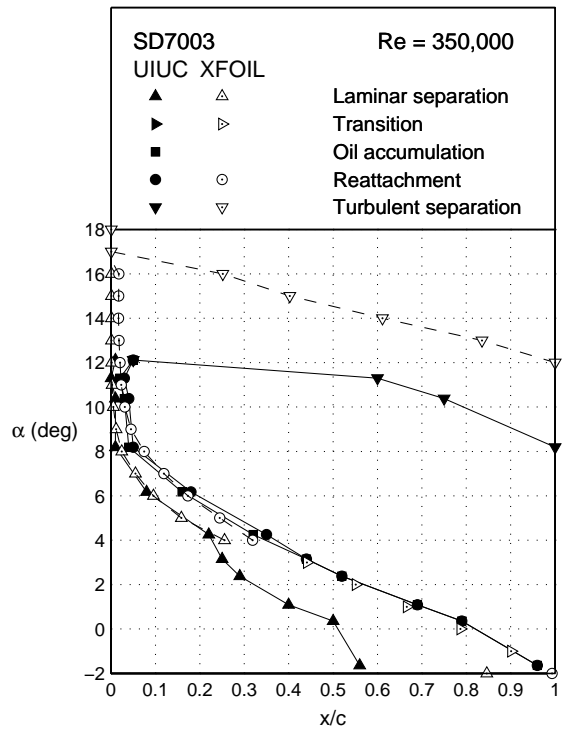

Fig. 35 Comparisons between computational and experimental location of upper surface flow features for the S8036, $Re = 500,000$.

Fig. 37 Comparisons between computational and experimental location of upper surface flow features for the SD7003, $Re = 350,000$.
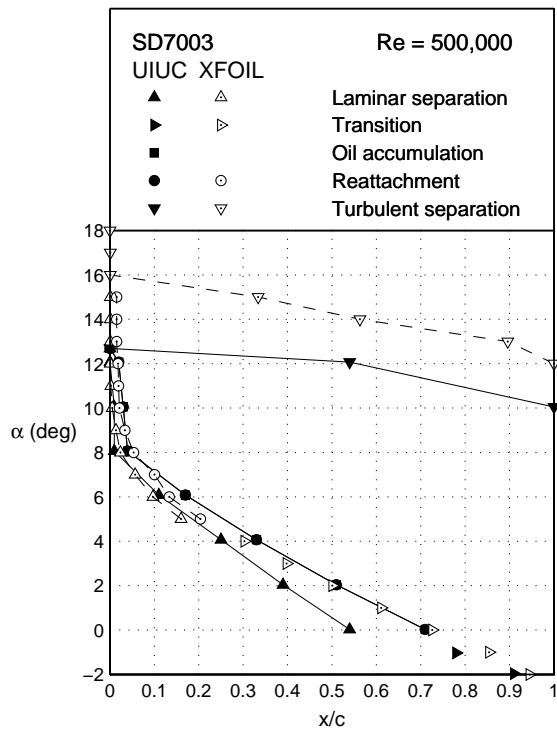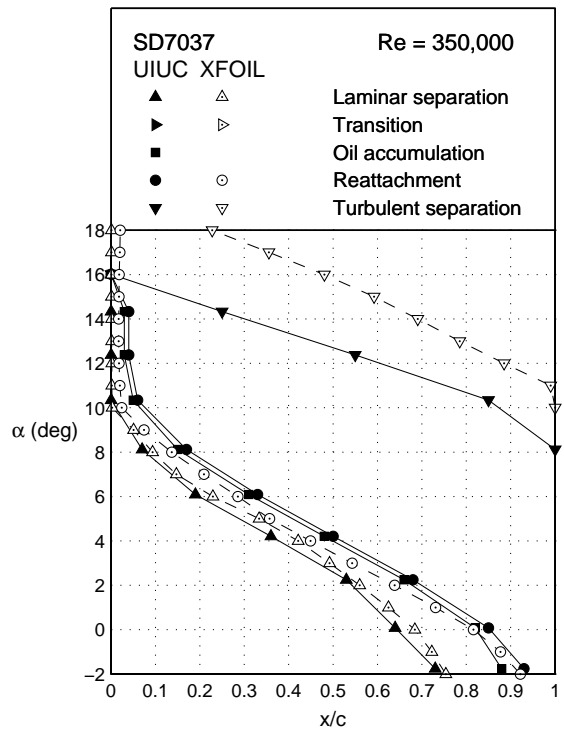
Fig. 38 Comparisons between computational and experimental location of upper surface flow features for the SD7003, $Re = 500,000$.

Fig. 40 Comparisons between computational and experimental location of upper surface flow features for the SD7037 (F), $Re = 350,000$.
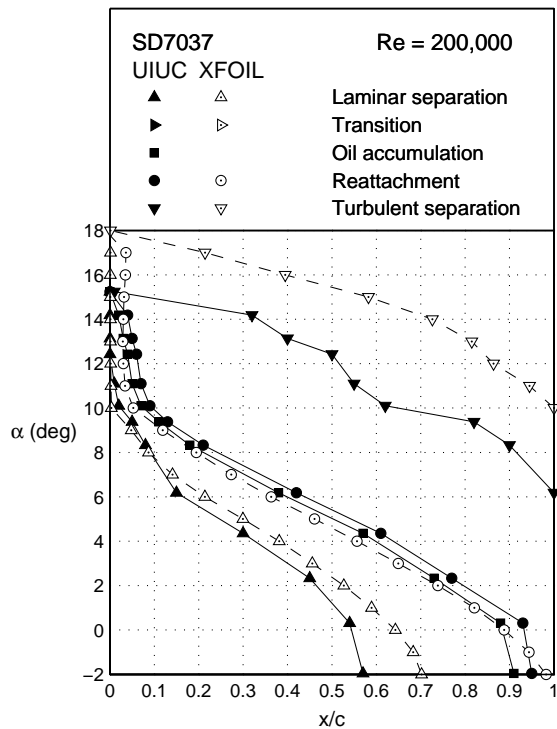

Fig. 39 Comparisons between computational and experimental location of upper surface flow features for the SD7037 (F), $Re = 200,000$.
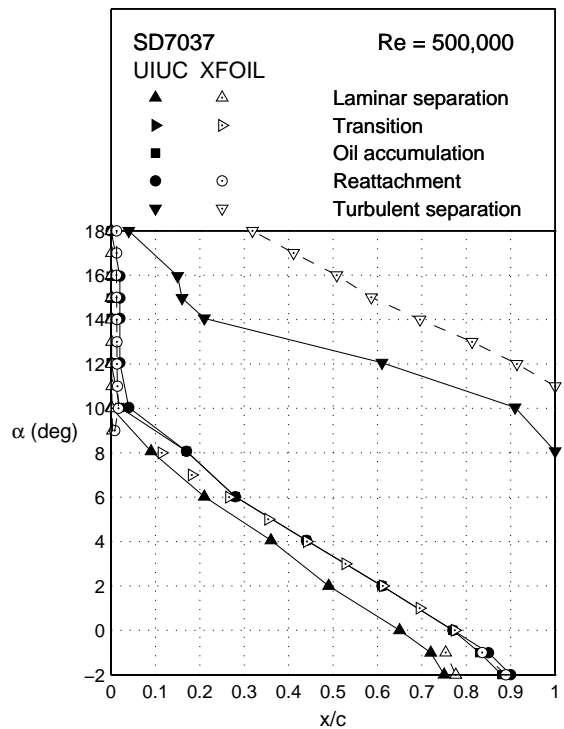

Fig. 41 Comparisons between computational and experimental location of upper surface flow features for the SD7037 (F), $Re = 500,000$.

For reference, Figs. 42–48 show the inviscid pressure distributions for the airfoils tested.

Summary

An extensive database of surface oil flow measurements has been documented on seven airfoils that represent a wide range in behavior at low Reynolds numbers. The measured surface oil flow results have
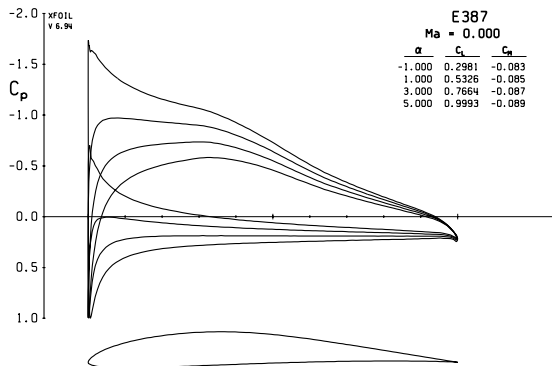

Fig. 42   Inviscid pressure distributions for the E387 airfoil.
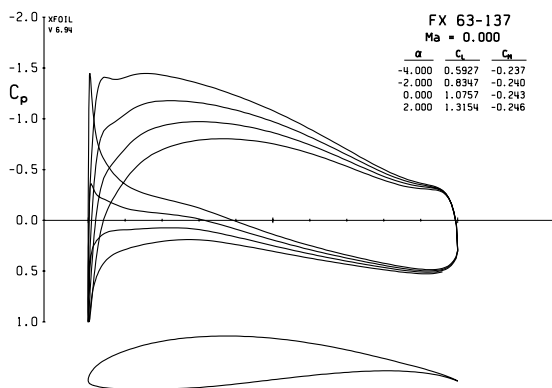

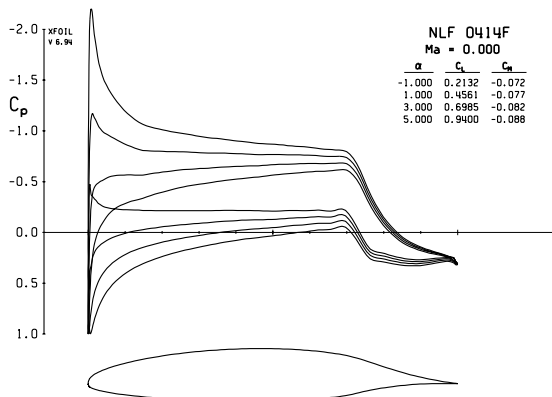Fig. 43   Inviscid pressure distributions for the FX 63-137 airfoil.

Fig. 44   Inviscid pressure distributions for the NASA NLF(1)-0414F airfoil.
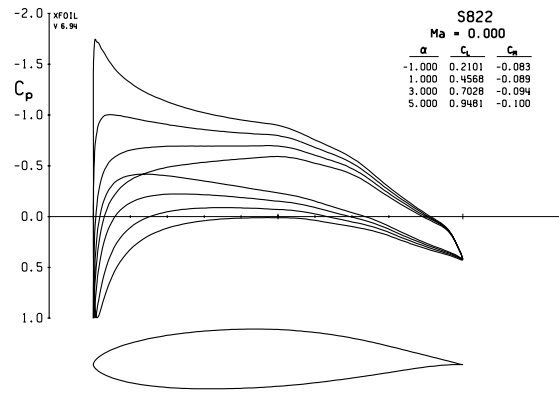

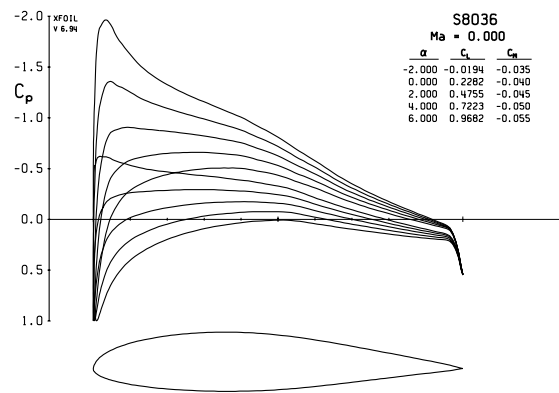Fig. 45   Inviscid pressure distributions for the S822 airfoil.

Fig. 46   Inviscid pressure distributions for the S8036 airfoil.
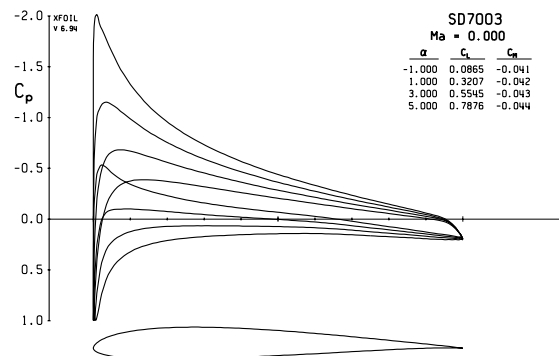
Fig. 47   Inviscid pressure distributions for the SD7003 airfoil.

been augmented by also acquiring airfoil performance data. The surface flow features have been compared to the predictions from XFOIL Version 6.94 ($n_{crit} = 9$). Some limited observations have been made and discussed briefly in this paper. It is hoped that this extensive database can be used to further validate and refine computational methods used for predicting low Reynolds number airfoil performance.

Fig. 48 Inviscid pressure distributions for the SD7037 airfoil.

Acknowledgments

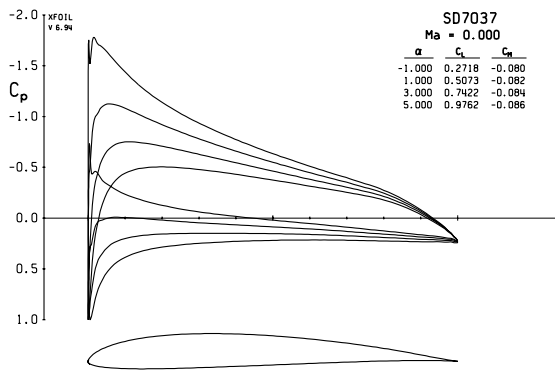The authors wish to thank Yvan Tinel and Mark Allen for their meticulous work in producing the wind tunnel models used in this study. Also the support from the National Renewable Energy Laboratory is gratefully acknowledged for partial support of this research. Finally, the authors gratefully acknowledge the helpful input from Benjamin A. Broughton during the course of this research.

References

[1] Selig, M. S., Guglielmo, J. J., Broeren, A. P., and Giguère, P., *Summary of Low-Speed Airfoil Data, Vol. 1*, SoarTech Publications, Virginia Beach, Virginia, 1995.

[2] Lyon, C. A., Broeren, A. P., Giguère, P., Gopalarathnam, A., and Selig, M. S., *Summary of Low-Speed Airfoil Data, Vol. 3*, SoarTech Publications, Virginia Beach, Virginia, 1998.

[3] Guglielmo, J. J. and Selig, M. S., "Spanwise Variations in Profile Drag for Airfoils at Low Reynolds Numbers," *Journal of Aircraft*, Vol. 33, No. 4, July–August 1996, pp. 699–707.

[4] Evangelista, R., McGhee, R. J., and Walker, B. S., "Correlation of Theory to Wind-Tunnel Data at Reynolds Numbers below 500,000," *Low Reynolds Number Aerodynamics*, edited by T. J. Mueller, Vol. 54 of *Lecture Notes in Engineering*, Springer-Verlag, New York, June 1989, pp. 131–145.

[5] McGhee, R. J., Walker, B. S., and Millard, B. F., "Experimental Results for the Eppler 387 Airfoil at Low Reynolds Numbers in the Langley Low-Turbulence Pressure Tunnel," NASA TM-4062, October 1988.

[6] Briley, R. W. and McDonald, H., "Numerical Prediction of Incompressible Separation Bubbles," *Journal of Fluid Mechanics*, Vol. 69, No. 4, 1975, pp. 631–656.

[7] Kwon, O. K. and Pletcher, R. H., "Prediction of Incompressible Separated Boundary Layers Including Viscous-Inviscid Interaction," *Transactions of the ASME*, Vol. 101, December 1979, pp. 466–472.

[8] Davis, R. L. and Carter, J. E., "Analysis of Airfoil Transitional Separation Bubbles," NASA CR-3791, July 1984.

[9] Walker, G. J., Subroto, P. H., and Platzer, M. F., "Transition Modeling Effects on Viscous/Inviscid Interaction Analysis of Low Reynolds Number Airfoil Flows Involving Laminar Separation Bubbles," ASME Paper 88-GT-32, 1988.

[10] Huebsch, W. W. and Rothmayer, A. P., "The Effects of Small-Scale Surface Roughness on Laminar Airfoil-Scale Trailing Edge Separation Bubbles," AIAA Paper 98-0103, January 1998.

[11] Alam, M. and Sandham, N. D., "Direct Numerical Simulation of 'Short' Laminar Separation Bubbles with Turbulent Reattachment," *Journal of Fluid Mechanics*, Vol. 403, 2000, pp. 223–250.

[12] Lin, J. C. M. and Pauley, L. L., "Low-Reynolds-Number Separation on an Airfoil," *AIAA Journal*, Vol. 34, No. 8, 1996, pp. 1570–1577.

[13] Drela, M., "XFOIL: An Analysis and Design System for Low Reynolds Number Airfoils," *Low Reynolds Number Aerodynamics*, edited by T. J. Mueller, Vol. 54 of *Lecture Notes in Engineering*, Springer-Verlag, New York, June 1989, pp. 1–12.

[14] Broeren, A. P. and Bragg, M. B., "Unsteady Stalling Characteristics of Thin Airfoils at Low-Reynolds Number," *Fixed and Flapping Wing Aerodynamics for Micro Air Vehicle Applications*, edited by T. J. Mueller, Vol. 195 of *AIAA Progress in Astronautics and Aeronautics*, June 2000.